J. Fluid Mech. (2012), *vol.* 698, *pp.* 335–357.
doi:10.1017/jfm.2012.88

Effective transition of steady flow over a square leading-edge plate

Mark C. Thompson†

Fluids Laboratory for Aeronautical and Industrial Research (FLAIR), Department of Mechanical and Aerospace Engineering, Monash University, Clayton, VIC 3800, Australia

(Received 17 June 2010; revised 21 September 2011; accepted 13 February 2012; first published online 30 March 2012)

Previous experimental studies have shown that the steady recirculation bubble that forms as the flow separates at the leading-edge corner of a long plate, becomes unsteady at relatively low Reynolds numbers of only a few hundreds. The reattaching shear layer irregularly releases two-dimensional vortices, which quickly undergo three-dimensional transition. Similar to the flow over a backward-facing step, this flow is globally stable at such Reynolds numbers, with transition to a steady three-dimensional flow as the first global instability to occur as the Reynolds number is increased to 393. Hence, it appears that the observed flow behaviour is governed by transient growth of optimal two-dimensional transiently growing perturbations (constructed from damped global modes) rather than a single three-dimensional unstable global mode. This paper quantifies the details of the transient growth of two- and three-dimensional optimal perturbations, and compares the predictions to other related cases examined recently. The optimal perturbation modes are shown to be highly concentrated in amplitude in the vicinity of the leading-edge corners and evolve to take the local shape of a Kelvin–Helmholtz shear-layer instability further downstream. However, the dominant mode reaches a maximum amplitude downstream of the position of the reattachment point of the shear layer. The maximum energy growth increases at 2.5 decades for each increment in Reynolds number of 100. Maximum energy growth of the optimal perturbation mode at a Reynolds number of 350 is greater than 10^4, which is typically an upper limit of the Reynolds number range over which it is possible to observe steady flow experimentally. While transient growth analysis concentrates on the evolution of wavepackets rather than continuous forcing, this appears consistent with longitudinal turbulence levels of up to 1 % for some water tunnels, and the fact that the optimal mode is highly concentrated close to the leading-edge corner so that an instantaneous projection of a perturbation field from a noisy inflow onto the optimal mode can be significant. Indeed, direct simulations with inflow noise reveal that a root-mean-square noise level of just 0.1 % is sufficient to trigger some unsteadiness at $Re = 350$, while a 0.5 % level results in sustained shedding. Three-dimensional optimal perturbation mode analysis was also performed showing that at $Re = 350$, the optimal mode has a spanwise wavelength of 11.7 plate thicknesses and is amplified 20 % more than the two-dimensional optimal disturbance. The evolved three-dimensional mode shows strong streamwise vortical structures aligned at a shallow angle to the plate top surface.

Key words: absolute/convective instability, nonlinear instability, separated flows

† Email address for correspondence: mark.thompson@monash.edu

1. Introduction

Despite the successes of global stability analysis in predicting wake instabilities, circular cylinder wake transition being a prime example (Dušek, Fraunie & Le Gal 1994; Barkley & Henderson 1996, for the Hopf and three-dimensional transitions, respectively), over the last two decades it has been realized that global stability analysis is not always a good predictor of the experimentally observed stability of real flows, at least when the instability mode spectrum is dominated by only a few modes. For the mainstream fluid dynamics community, perhaps the genesis of this realization was the observation of the massive transient amplification of perturbations due to the non-orthogonality of linear eigenfunctions. This helped to explain the observed turbulent transition of pipe flows at $Re \simeq 2000$, and plane Couette flow at $Re \simeq 350$ which is globally stable at all Reynolds numbers (Butler & Farrell 1992; Reddy & Henningson 1993; Trefethen *et al.* 1993), also see reviews by Chomaz (2005) and Schmid (2007). Since then there have been many studies of flow geometries for which the experimental observations indicate that effective transition to unsteady flow occurs significantly below the critical Reynolds number for global instability. (Of course, it is true that it has been realized for a much longer time that convective instabilities could be triggered by upstream perturbations, and that flows past corners or edges are regions of high flow receptivity so that perturbing the flow at such points can lead to massive downstream amplification. For example, in his 1966 AGARD report, Gaster (1966) observed 'disturbances in the separated flow were travelling waves, which grew spatially along the shear layer'.)

A classic example is the flow over a backward-facing step. Kaiktsis, Karniadakis & Orszag (1996) examined unsteadiness and convective instabilities of the backward-facing step wake after an earlier paper (Kaiktsis, Karniadakis & Orszag 1991) had indicated an unsteady flow well below the transition Reynolds number predicted by other computer simulations. The discrepancy was traced to insufficient resolution in the numerical simulations triggering convective instability. Since then Barkley, Gomes & Henderson (2002) have shown that the initial wake transition from the steady separated flow is through a three-dimensional steady transition rather than quasi-periodic shedding, as is commonly seen in experimental flows. It was also shown that the two-dimensional flow is globally stable up to Reynolds number of $\sim$1500. The paper by Blackburn, Barkley & Sherwin (2008*a*) quantifies the growth of optimal perturbation modes, indicating that there is substantial amplification of perturbations as they convect along the separating shear layer, which in practice leads to effective early transition. They perform three-dimensional direct numerical simulation (DNS) on the flow perturbed by Gaussian noise at inflow and observe the quasi-periodic release of vortex structures from the shear layer at a downstream location near where the optimal modes reach maximal amplitude. Also, the observed frequency is consistent with the wavelength and convection speed of the optimal disturbance.

Marquet *et al.* (2008) examine a smoothed backward-facing step in terms of resonator and amplifier dynamics. In terms of resonator dynamics (or global instability) the wake undergoes an initial transition from two-dimensional steady flow to three-dimensional steady flow, as occurs for the standard backward-facing step. The amplifier dynamics, examining transient growth of optimal perturbation modes, is also similar. Exponential amplification of perturbations initially localized near the step occurs as they convect along the shear layer. Further downstream the optimal perturbation modes decay. The upshot is that the amplification rate of perturbations is high enough to dominate the much slower growth of the global instability, so that for moderate Reynolds numbers it is expected that the first mechanism may dominate the

flow dynamics. In a followup paper, Marquet *et al.* (2009) examine the problem in terms of direct and adjoint global modes, especially with a view to the implications for flow control.

Flows through stenotic geometries, i.e. past partial blockages in pipes or channels, show similar if not more extreme transient energy growth. Griffith *et al.* (2008) examined pipe flow through a symmetrical stenosis, both experimentally and numerically. The global stability analysis indicates that global steady three-dimensional transition takes place at Reynolds numbers much higher than the flow is observed to undergo effective transition in the experiments using the same geometries. For example, for a blockage ratio of 0.5, experiments indicate that chaotic flow is sustained at Reynolds numbers below 1000, while the global stability analysis indicates that the flow should remain stable for Reynolds number of more than 2000. Blackburn, Sherwin & Barkley (2008*b*) examine numerically a similar stenotic geometry in terms of transient growth of optimal perturbations and global instability. Their findings are similar, but explicitly show the huge increase in the transient growth rate as the Reynolds number is increased, in line with the experimental results of the previous authors. More recently, Griffith *et al.* (2010) show that the transient shear-layer flow structures observed in the experiments match well with the flow structures obtained by seeding a DNS with the optimal transient perturbation mode.

In an informative recent paper, Ehrenstein & Gallaire (2008) examine the optimal growth and global temporal modes for the boundary-layer flow over a smooth bump, which produces a downstream recirculation bubble. They find that the temporal modes undergo transition as a group at a particular Reynolds number depending on bump height, and they are localized near the reattachment point of the separation bubble. These modes have shifted frequencies, so that a sum of these unstable modes can lead to modulation or beating; the authors correlate this with the flapping that is observed in such separating and reattaching flow. The observed modulation of the shedding is indeed well predicted by the beating frequency of the temporal modes. This phenomenon appears to have been found previously for a seemingly very different problem of the stability of a falling liquid curtain (Schmid & Henningson 2002). Of some interest, the temporal modes closely resemble the optimal growth modes after they have advected to the reattachment zone, thus seemingly connecting the overall flow dynamics to both the global and optimal growth modes. Of course, this is perhaps not surprising given that the advecting optimal perturbation modes can be constructed from linear combinations of the damped global modes, and they should evolve towards the individual dominant damped global mode(s) as they move far downstream. The temporal mode analysis by Cherubini, Robinet & Palma (2010) for the separated flow over a flat plate induced by blowing and suction shows a similar result. They also find that shear-layer flapping leading to large-scale vortex shedding from the mean separation zone can be correlated with temporal modes becoming unstable as a group. The linear interaction of this group of modes leads to regenerating wavepackets, which can be directly associated with the flapping. In addition, they find a structural change to the recirculation bubble close to the Reynolds number at which the temporal modes become unstable. This appears to introduce a second frequency to the flapping, which is apparent in their DNSs.

The aim of the current paper is to examine the flow over a different geometry, that of a long flat plate with a square leading-edge. Relative to the geometries examined above, the flow near the leading-edge corner is more highly accelerated. The flow has been examined before in terms of shear-layer receptivity near the leading edge. For example, a very small cross-stream flow oscillation is sufficient to lock the vortex

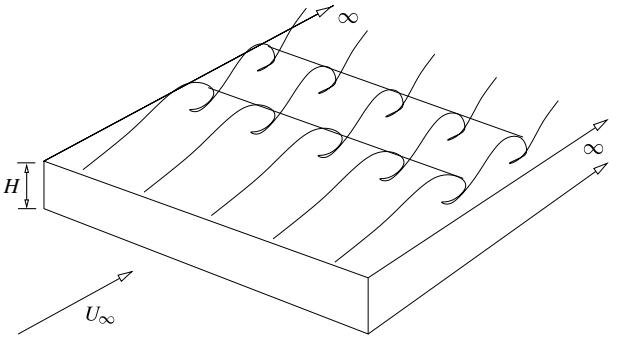

FIGURE 1. Problem setup: the plate is assumed to be semi-infinite in length and of infinite width. Above a certain Reynolds number the leading-edge separation bubble sheds semi-discrete vortices due to the receptivity of the leading-edge shear layer.

shedding from the separation bubble, and indeed severely shorten the mean bubble length (Tan, Thompson & Hourigan 1998; Mills, Sheridan & Hourigan 2003; Tan, Thompson & Hourigan 2004). In addition, for plates of particular length to height aspect ratios, the passage of vortices past the trailing edge can trigger a shear-layer perturbation at the leading-edge corners, resulting in subsequent shear-layer roll-up and shedding. A feedback loop can be established resulting in a discrete number of vortices on each side of the plate, with the number depending on the aspect ratio (Ohya *et al.* 1992; Hourigan, Thompson & Tan 2001). Thus, the sensitivity of the shear-layer near the leading edge corners is well established; however, an analysis in terms of transient growth of optimal perturbations has not yet been undertaken. This does throw further light on the flow dynamics for this case.

2. Methodology

The flow under investigation is shown in figure 1. The geometry is a long flat plate with a square leading edge. Ideally the plate is of infinite length so that there is no feedback to the leading-edge shear layers as shed vortices pass the trailing edge. The plate is also ideally infinitely wide. Above a Reynolds number of $\sim Re = U_\infty H/\nu = 100$, a separation bubble is formed as the shear layer separates from the leading-edge corner. Experiments indicate that at higher Reynolds numbers of $Re \sim 300$–400, quasi-periodic vortex shedding from the separating shear layer begins to occur. These vortical structures appear to become three-dimensional soon after forming (Sasaki & Kiya 1991), although that is not the focus of this paper, which concentrates on the initial predominantly two-dimensional release of vortices.

The flow is governed by the incompressible Navier–Stokes equations coupled with the continuity equation

$$\frac{\partial \boldsymbol{u}}{\partial t} + \boldsymbol{u} \cdot \boldsymbol{\nabla} \boldsymbol{u} = -\boldsymbol{\nabla} p + \nu \nabla^2 \boldsymbol{u}, \tag{2.1}$$

and

$$\boldsymbol{\nabla} \cdot \boldsymbol{u} = 0. \tag{2.2}$$

Here as usual p is the kinematic pressure, i.e. the pressure divided by the density, ν is the kinematic viscosity and $\boldsymbol{u}$ is the velocity vector. For the flows studied here, the flow variables are split into a two-dimensional base flow $(\bar{\boldsymbol{u}}(x, y), \bar{p}(x, y))$ and

perturbation fields $(\boldsymbol{u}'(t,x,y,z), \bar{p}'(t,x,y,z))$. The base flow, denoted by the barred quantities, satisfies the Navier–Stokes equations as do the full fields, allowing the equations for the perturbation fields to be extracted, which on linearizing are

$$\frac{\partial \boldsymbol{u}'}{\partial t} + \bar{\boldsymbol{u}} \cdot \boldsymbol{\nabla} \boldsymbol{u}' + \boldsymbol{u}' \cdot \boldsymbol{\nabla} \bar{\boldsymbol{u}} = -\boldsymbol{\nabla} p' + \nu \nabla^2 \boldsymbol{u}', \tag{2.3}$$

and

$$\boldsymbol{\nabla} \cdot \boldsymbol{u}' = 0. \tag{2.4}$$

The spatial derivatives in this case may include the z-dependent terms.

In this paper the focus is on transient growth of optimal disturbances, as previously examined for other flow geometries (e.g. Butler & Farrell 1992; Blackburn *et al.* 2008*a*; Ehrenstein & Gallaire 2008; Griffith *et al.* 2010). The analysis presented uses the approach described in various papers including Butler & Farrell (1992), Mamun & Tuckerman (1995) and Barkley, Blackburn & Sherwin (2008), and so only a brief overview is given here. The aim is to determine the maximum energy growth of an initial perturbation for a chosen time period. This can be expressed as an eigenvalue problem in which the perturbation can be expressed in terms of a set of optimal perturbation modes which grow to different amplitudes over the chosen time interval. These growth amplitudes effectively represent the associated eigenvalues. Even though the base flow may be globally stable, the non-normality of the global modes can lead to massive amplification of perturbations, i.e. massive transient growth. The relative energy amplification of an optimal mode is written as

$$G(\tau) = \frac{\mathscr{E}(t=\tau)}{\mathscr{E}(t=0)}, \tag{2.5}$$

where $\mathscr{E}(t) = (1/2)\int (u'^2 + v'^2 + w'^2)\,\mathrm{d}\mathscr{V}$ is the kinetic energy per unit mass in the perturbation velocity field at time t.

In practice, the determination of the optimal growth modes can proceed using the same time-stepping approach that can determine the linear stability of a steady base flow or the Floquet stability of time-periodic flows, i.e. integrating forward in time from a white noise perturbation field until only the dominant global modes remain. These can then be extracted based on a Krylov subspace approach using Arnoldi decomposition as described by Mamun & Tuckerman (1995), Barkley & Henderson (1996) and Barkley *et al.* (2008). For the optimal growth modes, the integration consists of two substeps: integrating the linear system forward in time until $t = \tau$; and then integrating the related adjoint linear system backwards in time, until $t = 0$. This can be repeated until the first few dominant optimal perturbation modes can be extracted to the desired accuracy. Note that here 'optimal mode' refers to the modes associated with the product of the forward and backward (adjoint) Navier–Stokes evolution operator, or alternatively the eigenvectors from the singular value decomposition of the evolution operator, as discussed in Barkley *et al.* (2008). The term 'dominant' refers to the optimal mode which is amplified maximally. However, in this paper the term 'first few dominant modes' is used. This indicates the modes with the highest growth factors (for a particular Reynolds number and growth time). 'Modes' can also refer to global instability modes depending on the context.

The equations are discretized in space using the spectral-element approach. The current implementation of the software has been applied previously to various related problems, such as the wakes of cylinders (Thompson, Hourigan & Sheridan 1996;

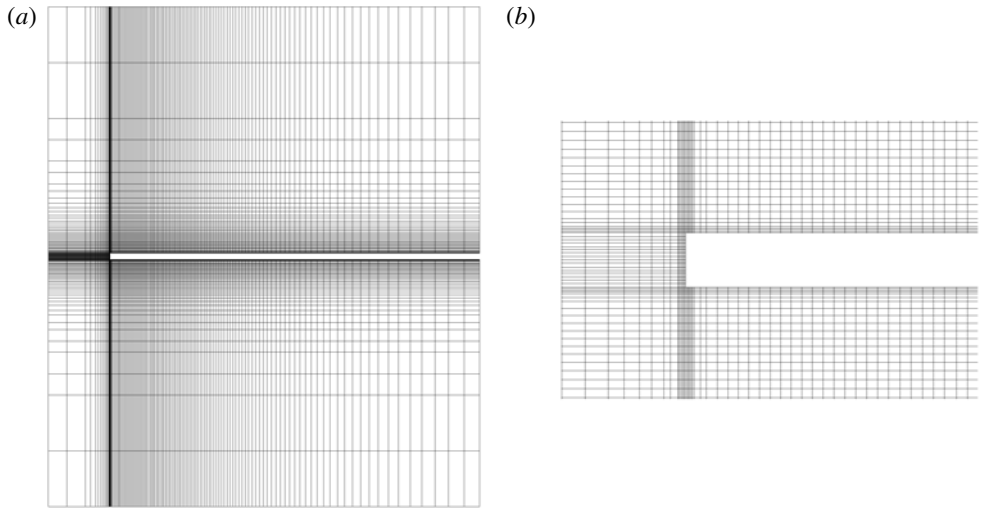

FIGURE 2. (*a*) Typical computational mesh employed for the time-dependent simulations. Only the macro-elements are shown. These elements are further subdivided into $n \times n$ nodes, where n is at least four for the current simulations. The inflow length is $10H$, the plate length is $60H$, top and bottom boundaries are at $\pm 40H$. (*b*) Zoomed view of mesh near leading-edge corners.

Thompson, Leweke & Williamson 2001*b*; Leontini, Thompson & Hourigan 2007), spheres (Thompson, Leweke & Provansal 2001*a*), tori (Sheard, Thompson & Hourigan 2003, 2004) and stenotic flows (Griffith *et al.* 2008, 2010). A fuller description of the spectral-element approach to linear stability analysis, including Floquet analysis, is provided in Ryan, Thompson & Hourigan (2005). In terms of the current problem, the extension to the code to extract optimal growth modes has been validated by comparison with predictions from Butler & Farrell (1992) and Blackburn *et al.* (2008*a*). The current implementation is based on the description in Thompson *et al.* (2006). A significant advantage of the spectral-element method is the ability to select the resolution at runtime by selecting the number of nodes in the macro-elements.

The temporal discretization employs a classical splitting scheme suggested by Chorin (1968); the current implementation is detailed in Karniadakis, Israeli & Orszag (1991). The nonlinear advection step is performed first, followed by the step accounting for the effect of the pressure gradient, which also imposes flow incompressibility, and finally the diffusion step. First-order pressure boundary conditions are imposed at the no-slip boundary at the surface of the plate (Karniadakis *et al.* 1991) and this leads to a velocity field that is second-order accurate in time and satisfies mass conservation at the no-slip boundaries. This temporal convergence behaviour has been established for the current code in previous studies. Also note that the Courant restriction on the time step generally means that more than 1000 time steps are required per shedding period (for the unsteady case).

This problem is relatively expensive in computational terms because of the sizeable regions with large velocity gradients requiring high resolution. In particular, there are geometric singularities at the leading-edge corners and relatively fine boundary layers extending all of the way to the outflow boundary. The leading-edge corners are particularly demanding since the velocity gradient near that region is very high as the shear layer separates there.

Figure 2 shows the spectral-element mesh used for the simulations. Note that only macro-elements are shown. Internally macro-elements are further subdivided into $n \times n$ node points. For the simulations presented in the paper, n is at least four. The mesh concentration is particularly high in the neighbourhood of the leading-edge corners to resolve the separating shear layers, and close to the plate to resolve the vortical structures as they convect downstream. Overall this mesh employs 12 080 macro-elements. The cross-stream boundaries are set at 40 step heights from the plate, giving a blockage ratio of 1.25 %. The upstream and outflow boundaries are situated $10H$ and $60H$ from the leading-edge, respectively. At the upstream and side boundaries, the velocity is set to U_∞ and at the outflow boundary $\mathrm{d}\boldsymbol{u}/\mathrm{d}n = 0$. For the optimal perturbation mode simulations the perturbation velocity is set to zero at all computational boundaries, for the reasons discussed in Barkley *et al.* (2008).

This mesh is the final of a sequence of meshes examined to verify resolution and domain size to accurately capture the flow dynamics. An initial mesh was constructed based on experience from similar problems. For that mesh the resolution was found to be inadequate both near the leading-edge corners and in the boundary layers. Since the spectral-element approach is only C_0 continuous at element boundaries, this can easily be discerned from whether the vorticity, i.e. a derivative of the velocity, is continuous across element boundaries for a reasonable internal resolution. Four meshes were constructed before a satisfactory compromise between localized mesh concentration and total mesh points was achieved. Increasing the internal resolution can then be systematically investigated to determine the nodes per element required to fully resolve the flow (i.e. better than 1 % in quantities such as the force coefficients, critical Reynolds numbers or pointwise velocity components). There was some effort to ensure the outflow boundary was placed sufficiently far downstream such that it was not unphysically affecting the results. To do this the outflow length was increased from $30H$ to $60H$, and it was verified that this did not affect growth multipliers for the optimal perturbation analysis by more than 1 %. However, because some simulations were performed to extract global temporal modes at higher Reynolds numbers ($Re > 500$), for which the reattachment length is considerably longer, it was decided to maintain the longer outflow length for all of the simulations. Finally, the influence of the inflow length was also investigated. A test for $Re = 350$ and $\tau = 24$ indicated that doubling the inflow length also resulted in less than a 1 % change to the calculated growth multiplier.

3. Results

3.1. *Two-dimensional baseflow*

As described in the introduction above, this flow is very sensitive to external perturbations. For finite-length plates, at Reynolds numbers above a few hundred, the passage of vortices from the leading edge past the trailing edge is sufficient to maintain a feedback loop maintaining strong leading-edge shedding (Nakamura, Ohya & Tsurata 1991; Ozono *et al.* 1992; Hourigan *et al.* 2001). For certain plate lengths, the phasing of leading-edge vortices passing the trailing edge is such that the timing of the induced perturbation at the upstream separating shear layer leads to strictly periodic shedding. For each of these preferred lengths there is a discrete but different number of vortices between the leading and trailing edge. In between these preferred plate lengths the timing of pressure pulses supporting this feedback loop does not lead to a purely periodic shedding (Ozono *et al.* 1992; Tan *et al.* 1998). The case studied here is that of a semi-infinite plate so that this feedback mechanism does not

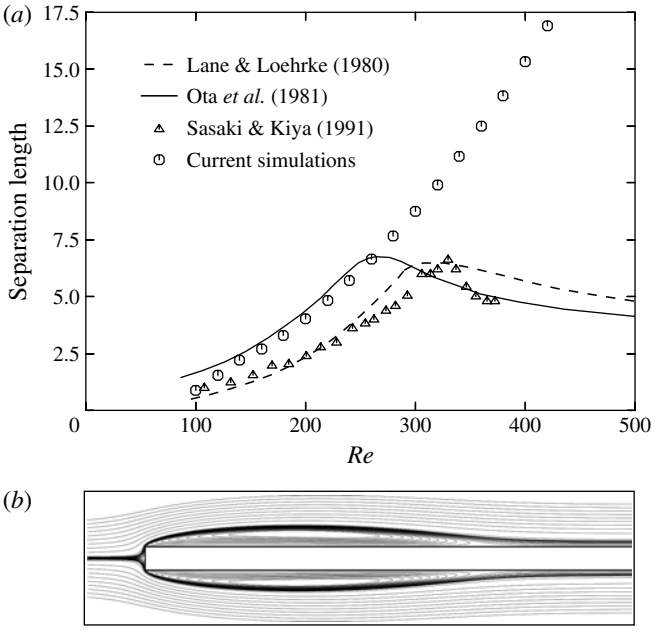

FIGURE 3. (*a*) Reattachment length of the separation bubble as a function of Reynolds number from various experimental studies. Where the experimental curves turn over, the flow undergoes transition to unsteady shedding. Reattachment lengths from the current simulations are also shown. (*b*) Streamlines showing the recirculation zones for $Re = 400$.

apply. In practice, this is difficult to achieve using a numerical model because the domain needs to be truncated at some point. This downstream truncation has a similar effect to using a finite-length plate, in that as the vortices exit the domain this can perturb the upstream shear layer causing it to roll up. The effect is lessened for longer plate lengths, since the extra outflow length allows the convecting vortices to diffuse more before they exit the domain. For the chosen domain outflow length of $60H$, the flow evolves smoothly to a steady state for Reynolds number up to greater than 450. At $Re > 500$, the flow does not approach an asymptotic steady state but rather the separation bubble sheds vortices quasi-periodically.

Figure 3 shows the behaviour of the reattachment length with Reynolds number in the steady flow regime. This figure also shows results from previous experimental studies (Lane & Loehrke 1980; Ota, Asano & Okawa 1981; Sasaki & Kiya 1991) for comparison. It shows that experimentally, the separation bubble becomes unsteady in the Reynolds number range $260 < Re < 330$ depending on the experiment. For higher Reynolds numbers, the separation length indicates the time-mean value, which asymptotes to be between 4–5H. Notably the current numerical predictions fall between the experimental results of Lane & Loehrke (1980), Ota *et al.* (1981) and Sasaki & Kiya (1991). Numerical simulations with higher resolution had no effect on the predictions of the separation bubble lengths to graphical accuracy.

3.2. *Global instability modes*

As indicated, the direct two-dimensional time-dependent simulations indicate that the flow remains steady up to a Reynolds number of ∼500. This is well past the point at which various experiments show that the flow is both unsteady and three-dimensional.

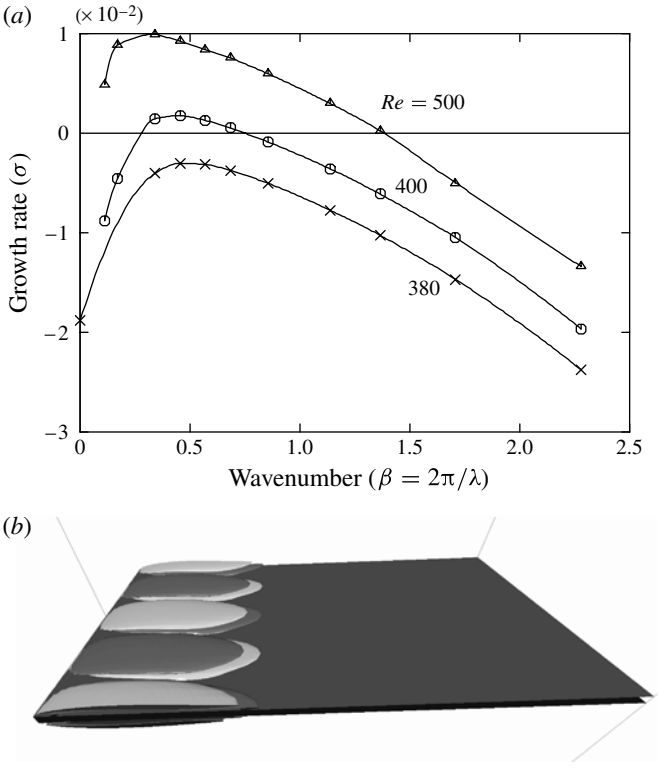

FIGURE 4. (*a*) Growth rate of the dominant three-dimensional mode as a function of the wavenumber for different Reynolds numbers for the global stability analysis. The dominant mode has a real growth rate, i.e. the three-dimensional transition occurs through a steady-to-steady transition. Interpolating the curves gives the transition Reynolds number as 393 corresponding to a spanwise wavelength of $15.7H$. (*b*) Depiction of the three-dimensional mode using isosurfaces of spanwise perturbation vorticity to highlight the mode structure. This case corresponds to $Re = 400$ and $\lambda_z = 15H$, which is close to the maximally amplified wavelength. Two wavelengths are shown for clarity.

A global linear stability analysis of the steady flow was performed to investigate the onset of three-dimensional flow. The results are shown in figure 4. Growth rate curves are plotted as a function of spanwise wavenumber for various Reynolds numbers. Three-dimensional transition occurs between $Re = 380$ and 400 through a 'regular' bifurcation, i.e. steady to steady flow. This is in line with the transition behaviour for the flow over a backward-facing step. In that case, the three-dimensional transition also occurs well before the transition to unsteady flow as shown by Barkley *et al.* (2002). Extrapolating between the curves at $Re = 380$ and 400 indicates that three-dimensional transition occurs at $Re_{crit} = 393$ at a spanwise wavelength of $15.7H$. This wavelength can be compared with those for a number of other similar geometries explored by other researchers. Barkley *et al.* (2002) found a critical wavelength of 6.9 step heights for the flow over a backward-facing step. The mode structure is similar, in that the unstable mode consists of counter-rotating cells when looking down from above. (See figure 10 of that paper.) In Gallaire, Marquillie & Ehrenstein (2006) for transition in the flow over a smooth bump, the steady three-dimensional mode had

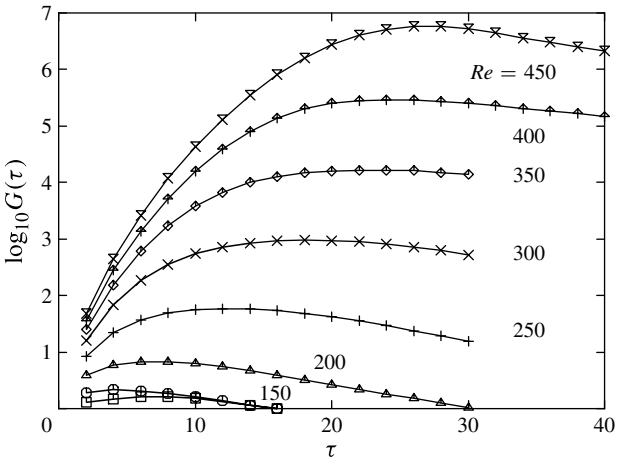

FIGURE 5. Energy amplification of the dominant two-dimensional perturbation mode as a function of non-dimensional time τ for various Reynolds numbers.

a critical wavelength ∼12.6 bump heights. Hence, the current analysis at least seems qualitatively consistent with the similarly long wavelengths found in previous studies.

Thus, both transition to steady three-dimensional flow and the transition to unsteady flow occur at significantly higher Reynolds numbers than the effective unsteady, three-dimensional transition seen in experiments.

3.3. *Optimal growth solutions*

As discussed above, the sensitivity of this flow to perturbations is well known. Apparently similar flows such as stenotic flow (Blackburn *et al.* 2008*b*; Griffith *et al.* 2008), flow over a backward-facing step (Blackburn *et al.* 2008*a*) and flow over a bump (Marquet *et al.* 2008) show substantial energy amplification of optimal perturbation modes for moderate Reynolds numbers. Superficially at least these flows are similar in that there is an attached recirculation region bounded by a no-slip boundary on one side and a thin shear layer emanating from a separation point on the other. A small perturbation initially located near the separation point can undergo significant amplification as it advects along the shear layer.

The situation can be quantified by determining the set of perturbation modes that result in maximal growth over a given time interval τ. This can be done for different time intervals and different Reynolds numbers resulting in the energy amplification factor ($G(\tau, Re)$) of the dominant mode shown in figure 5. As the Reynolds number increases, for the same advection time, there is a rapid increase in the energy amplification of the dominant mode. For $Re = 450$, the energy growth is almost seven orders of magnitude, indicating why it is difficult to obtain a steady flow at such Reynolds numbers in experiments, since the projections of background noise onto the optimal growth modes amplify to large levels as they are advected with the flow. The maximum growth occurs for larger values of τ as the Reynolds number increases. This is consistent with the increase in separation bubble length with Reynolds number. The perturbation mode is amplified in the shear layer as it traverses the separation zone. Further downstream the mode decays, consistent with the fact that the flow is globally stable at these Reynolds numbers. Figure 6 shows a close up of the perturbation energy field for the dominant optimal mode for $Re = 350$ and $\tau = 24$ in

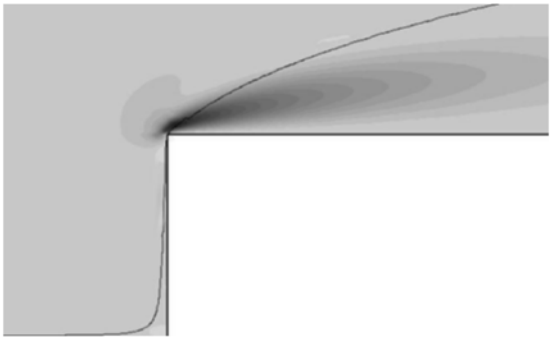

FIGURE 6. Shaded contour plot of the local perturbation energy of the optimal two-dimensional mode for $Re = 350$, $\tau = 24$, showing the perturbation is concentrated at the leading-edge corner.

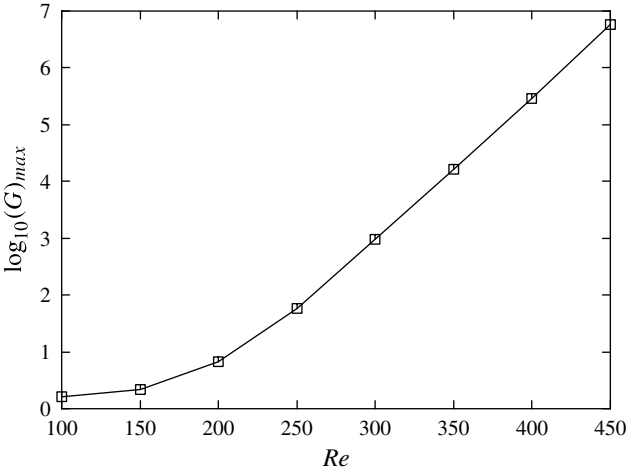

FIGURE 7. Maximum energy amplification as a function of Reynolds number from optimal growth analysis assuming two-dimensional perturbations.

the vicinity of leading-edge corner. The maximum amplitude occurs close to the shear-layer separation point at the leading-edge corner. Note that the maximum amplitude of the downstream pointing lobe is directed along the bisector of the recirculation zone. Outside of the region depicted in the figure the amplitude of the mode is low.

Figure 7 shows the maximum energy amplification with respect to τ at each Reynolds number as a function of the Reynolds number. The slope of the curve is approximately linear above $Re = 250$, with a gradient of 2.5×10^{-2}, i.e. 2.5 orders of magnitude energy growth for a Reynolds number increase of 100.

Figure 8 indicates how the different optimal modes corresponding to different values of τ relate. The perturbation vorticity fields are shown for $\tau = 2$ and $\tau = 24$, both for a Reynolds number of 350. The latter is close to the time interval that gives maximum amplification as can be seen from the figure, which also shows the envelope curve indicating the maximum amplification for each value of τ. The perturbation fields for the two cases both indicate that the initial distribution leading to optimal growth is

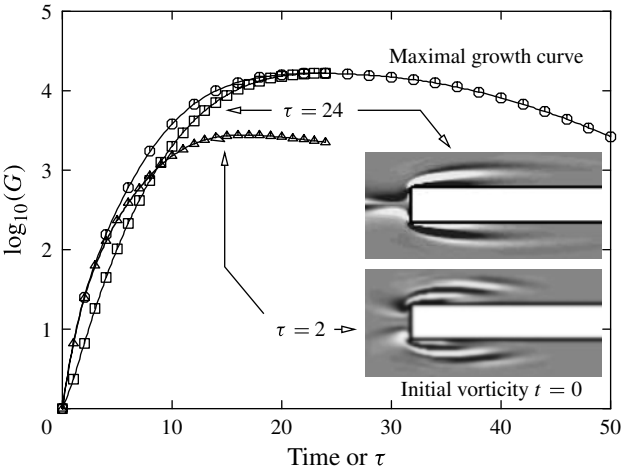

FIGURE 8. The evolution of the perturbation energy with time for the optimal two-dimensional modes corresponding to $\tau = 2$ and $\tau = 24$, for $Re = 350$. The maximal growth curve is also plotted for comparison. The initial vorticity fields for the two modes are shown in the insets.

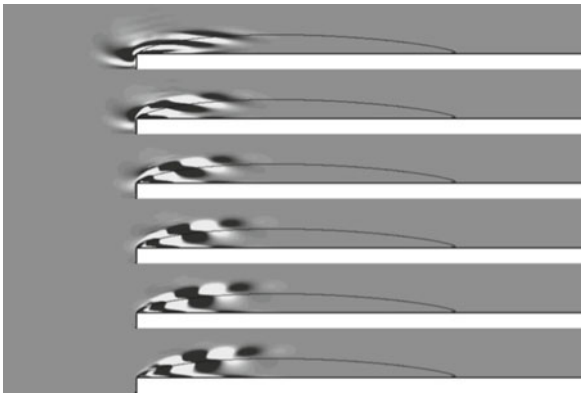

FIGURE 9. Evolution of the optimal two-dimensional initial disturbance with time for $\tau = 2$ and $Re = 350$. Times correspond to $t = 0$, 0.4, 0.8, 1.2, 1.6 and 2.0. The solid line indicates the separating streamline. Only the top half of the domain is shown to save space. The downstream boundary is at $x = 16H$.

concentrated close to the leading edge of the plate. The field for the smaller value of τ has a shorter wavelength, or at least leads to a shorter wavelength as the field advects downstream as shown in figures 9 and 10. This is consistent with the thinner shear layer close to the separation point. That is, it can be related to the fact that the preferred Kelvin–Helmholtz instability wavelength scales on the thickness of the shear layer. Thus, this perturbation field grows quickly initially but further downstream as the shear layer thickens, it grows more slowly than a longer wavelength perturbation would. Consequently, for larger τ, it should be expected that the effective optimal mode wavelength would be longer. This behaviour is borne out by the amplification curves for the two cases, showing the growth of both initial perturbation fields with time.

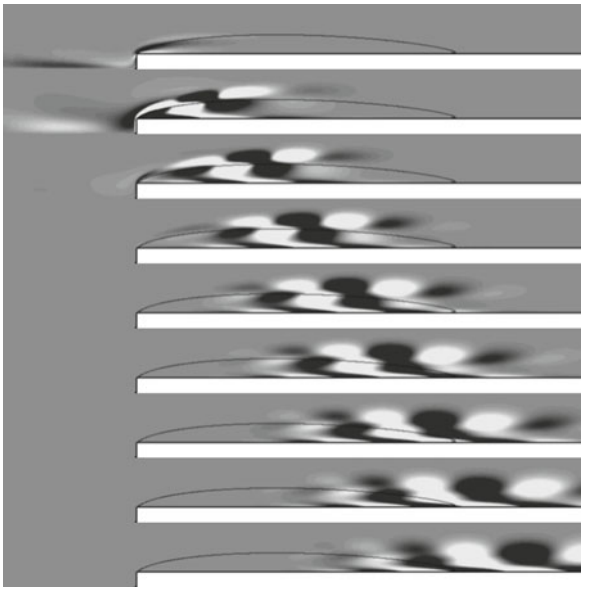

FIGURE 10. Evolution of the optimal two-dimensional initial disturbance with time for $\tau = 24$ and $Re = 350$. Times correspond to $t = 0, 3, 6, 9, 12, 15, 18, 21$ and 24. The solid line indicates the separating streamline. Only the top half of the domain is shown to save space. The apparently large amplitude of the mode upstream of the leading edge is slightly misleading, and due to the choice of contour levels. The mode amplitude is maximum close to the leading-edge corner as indicated in figure 6. The downstream boundary is at $x = 16H$.

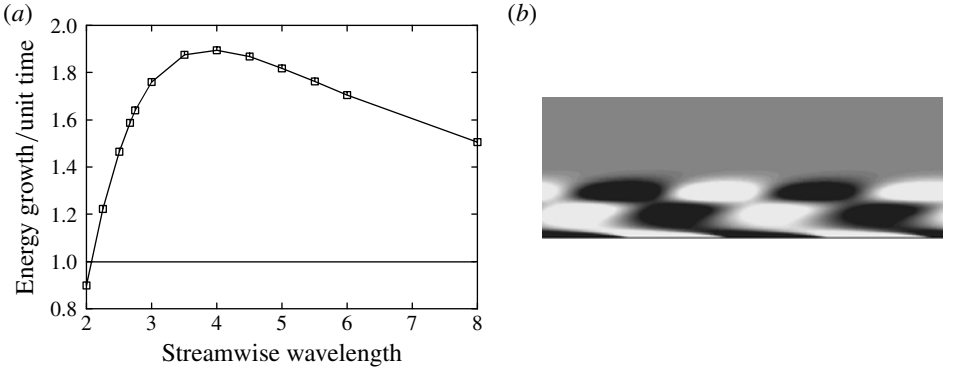

FIGURE 11. (*a*) Energy growth per unit time for the two-dimensional linear stability mode based on the velocity profile taken through the centre of the separation bubble ($x/H = 5.33$) as a function of streamwise wavelength (λ_x/H) for $Re = 350$. (*b*) Vorticity distribution for the linear mode with $\lambda_x/H = 4$, which is close to the most amplified wavelength.

To explore this further, the one-dimensional linear stability of the horizontal velocity profile taken through the middle of the separation bubble was determined, in spite of the fact that the flow is not closely one-dimensional and that the whole separation bubble could not contain many wavelengths. Figure 11 shows the energy growth

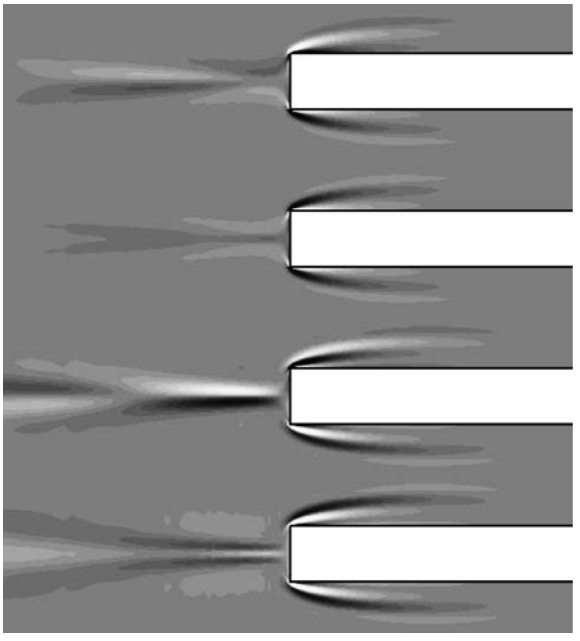

FIGURE 12. The first four two-dimensional optimal growth modes at $Re = 350$ for $\tau = 24$, which gives close to the maximum energy growth for this Reynolds number.

rate as a function of the streamwise wavelength. The fastest growing mode has a wavelength of approximately $\lambda_x = 4H$. The corresponding frequency is 0.115. The spanwise perturbation vorticity distribution is shown at the right of this figure. This shows that the instability is basically a Kelvin–Helmholtz mode slightly modified at the no-slip boundary by the presence of the boundary. Clearly the mode shape is very similar to the vorticity distribution of the optimal perturbation mode after it has advected to the middle of the bubble (see the fourth image of figure 10). At that time ($t = 9$), the effective wavelength of the perturbation wavepacket is close to $3H$, although the entire wavepacket only consists of about two wavelengths. The figure shows that for $\lambda_x = 3H$ the one-dimensional linear mode is still strongly amplified, with the growth rate less than 10 % below the maximum value. Indeed, it should be expected that the optimal mode wavelength would be less than the preferred one-dimensional linear stability wavelength because as the optimal mode traverses the shear layer upstream of the middle, the thinner shear layer will lead to higher amplification of shorter wavelengths. The energy amplification rate of the optimal perturbation mode at $t = 9$ is approximately 1.5; this is not far below the value of 1.8 for the idealized convective mode for $\lambda_x = 3H$ shown in figure 11.

Figure 12 shows the first four optimal growth modes for $Re = 350$ and $\tau = 24$. The mode shapes are similar, with the perturbation field concentrated near the leading edge. The first two modes are effectively an antisymmetric and symmetric version of the same mode, and similarly for the third and fourth modes. The growth multipliers for these modes are 1.664, 1.654, 1.325 and 1.227×10^4, respectively. Figure 13 shows the evolved perturbation field at $t = 24$ for the first two modes. Again, these are effectively antisymmetric and symmetric versions of the same mode.

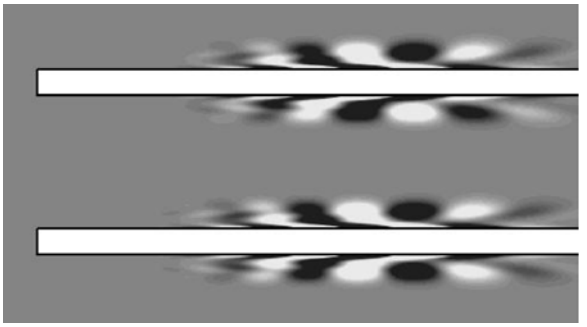

FIGURE 13. Vorticity fields corresponding to the evolution of the first two optimal modes at $Re = 350$ for $t = \tau = 24$. The downstream boundary is at $x = 20H$.

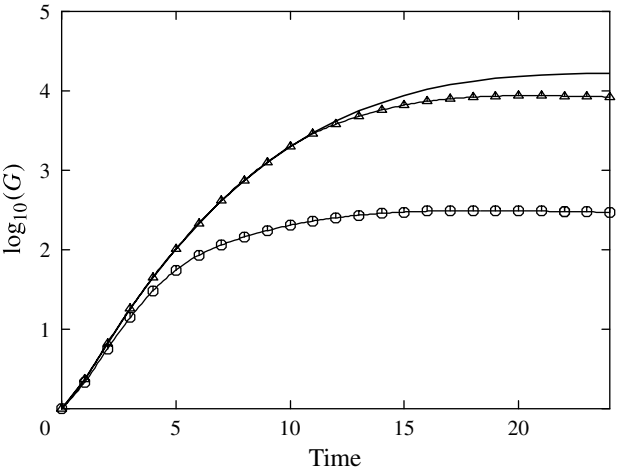

FIGURE 14. Energy amplification of two-dimensional optimal modes for finite amplitude disturbances due to nonlinear saturation. The initial mode corresponds to $\tau = 24$, $Re = 350$. The triangles correspond to a perturbation level of $\sim$3 % and the circles to a perturbation level of 30 %. The results for the 0.3 % case lie on the solid line. Refer to the text for details.

3.3.1. *Nonlinear saturation*

Figure 14 shows the effect of saturation of a finite-amplitude optimal perturbation as it advects downstream. This figure shows the relative energy growth of the perturbation field extracted from a direct simulation of the steady flow seeded with the dominant optimal perturbation mode corresponding to $\tau = 24$ and $Re = 350$. Different amplitudes of the optimal mode are used to perturb the initial steady flow. To quantify this, the maximum local specific kinetic energy at any point in the domain for the steady base flow is 0.774 units, and the upstream flow specific energy is 0.5 units, since the background velocity is set to 1 unit. The optimal mode amplitude is only significant near the leading edge of the plate as indicated in figure 6. The maximum local specific energy of the arbitrarily scaled optimal mode used for the reference case is 0.453×10^{-3} units, which occurs close to the leading-edge corner. Figure 14 shows the actual growth from perturbing the initial steady flow with the optimal mode at the reference level (triangles) and 100 times the reference level (circles). The optimal

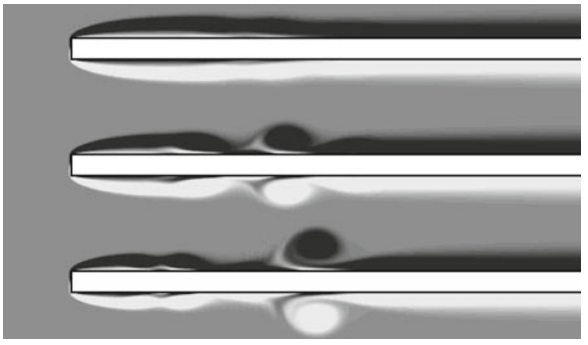

FIGURE 15. The effect of perturbing the flow with the optimal mode at different perturbation amplitudes. The vorticity field at $t = 15$ is shown for perturbation levels of 0.3, 3 and 30 %. The two-dimensional disturbance used to perturb the flow corresponds to the dominant growth mode for $\tau = 24$ and $Re = 350$. The downstream boundary is at $x = 25H$. See the text for further details.

growth curve is shown for comparison. Thus, for the first case the maximum local energy is at a relative level of $\sim 10^{-3}$, i.e. the maximum local velocity perturbation is approximately $\sqrt{10^{-3}} \sim 1/30$, or $\sim 3\,\%$. Similarly, for the more highly perturbed case, the maximum local perturbation is $\sim 30\,\%$. Figure 15 shows the evolved vorticity for the full flow field at $t = 15$ for maximum perturbation amplitudes of 0.3, 3 and 30 % of the base velocity. The lowest amplitude case effectively shows the induced linear perturbation to the otherwise steady vorticity field caused by the linear growth of the optimal perturbation mode as the perturbation advects downstream. The two high-amplitude cases show the nonlinear saturation of the perturbed flow. The main outcome of the nonlinear evolution of the optimal mode is, not surprisingly, the development of a strong vortex roller, as typically seen in experiments at this and higher Reynolds numbers (e.g. see the references given in figure 3). These results also seem to be broadly consistent with the fact that experimentally it is not possible to observe a steady flow at Reynolds numbers higher than ~300–350 (again see the references shown in figure 3), despite the fact that the flow is globally linearly stable at such Reynolds numbers and indeed much higher Reynolds numbers (see further analysis below).

3.3.2. *Three-dimensional optimal growth modes*

Up to this point, the optimal growth has been examined assuming that the perturbation field is two-dimensional. Of course, it is not necessarily the case that a two-dimensional perturbation gives the highest growth. The analysis extends to examine three-dimensional optimal modes assuming a sinusoidal spanwise dependence. Figure 16 shows the prediction of the energy amplification against τ for different spanwise wavelengths at $Re = 350$. Clearly, a two-dimensional mode does not give maximum growth. Further analysis using quadratic interpolation from results for longer wavelengths indicates that for $Re = 350$, the maximum amplification occurs for a spanwise wavelength of $11.7H$ at $\tau = 26$. The corresponding energy amplification factor is 0.200×10^5, which is only $\sim 20\,\%$ larger than the maximum for a two-dimensional mode of 0.165×10^5.

The initial perturbation field of the three-dimensional modes are very similar to the optimal two-dimensional perturbation fields, at least in terms of spanwise

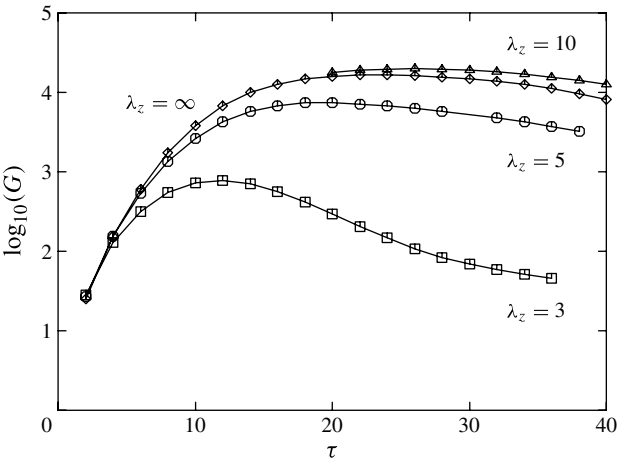

FIGURE 16. Energy amplification of the dominant three-dimensional transient mode as a function of non-dimensional time τ for $Re = 350$. The different curves correspond to different spanwise wavelengths. Note that the $\lambda_z = 10$ curve overlays the $\lambda_z = \infty$ curve for lower values of τ, but this part has not been drawn to reduce clutter.

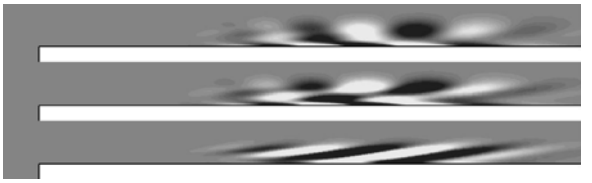

FIGURE 17. Comparison of the evolved two-dimensional and three-dimensional optimal perturbation modes for $Re = 350$, $\tau = 24$ and $t = 24$. Top and middle images show the spanwise perturbation vorticity field for the two-dimensional and three-dimensional cases. The lower image shows the streamwise perturbation vorticity for the three-dimensional case. The downstream boundary is at $x = 20H$.

perturbation vorticity. However, there are some differences which become visible as the perturbation field evolves as it advects downstream. Figure 17 shows the spanwise perturbation vorticity of the evolved fields for $Re = 350$, $\tau = 24$, at $t = 24$ for the two-dimensional (top) and three-dimensional (middle) cases. The lower image shows streamwise perturbation vorticity for the three-dimensional mode. For the three-dimensional analysis, the spanwise wavelength is $10H$. For the spanwise vorticity images, the fields show similar vortical structures near the plate boundary and further away, but in between the middle image shows that like signed vorticity is connected together. The streamwise perturbation vorticity for the three-dimensional case shows a set of elongated angled vorticity structures. Possible physical generation mechanisms for similar flows have been discussed in various papers (Pauley, Moin & Reynolds 1990; Alam & Sandham 2000; Jones, Sandberg & Sandham 2008; Marquet *et al.* 2009; Marxen & Rist 2010). Figure 18 provides three-dimensional visualizations for the spanwise and streamwise vortical structures for the three-dimensional case.

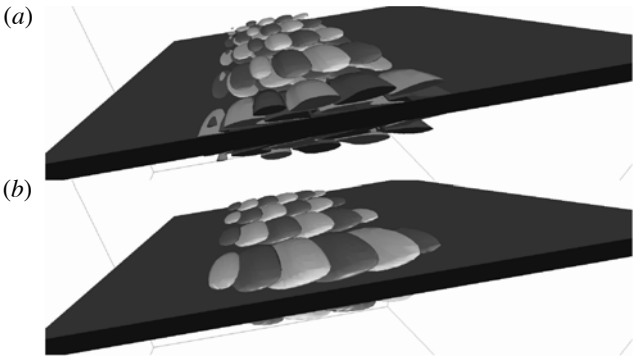

FIGURE 18. Visualizations of the perturbation spanwise (*a*) and streamwise (*b*) vortical structures for the evolved dominant optimal perturbation mode. Here $Re = 350$, $\tau = 24$, $t = 24$ and $\lambda_z = 10H$. Flow is left to right and two wavelengths are shown.

3.4. *Growth from triggering by different types of disturbances*

Real flows, of course, are subject to a variety of disturbances that may perturb the flow and substantially alter the behaviour of the flow from the ideal case. Examples include flow turbulence, acoustic perturbations and structural vibration, and flow-induced vibration. In numerical simulations, low resolution can lead to premature triggering of convective instabilities (Kaiktsis *et al.* 1991). For the geometry here, the effect of low-level noise at the inflow is considered, such as was examined previously, e.g. by Blackburn *et al.* (2008*a*) for the backward-facing step. Of course, it should be borne in mind that the main emphasis of the paper is on transient growth analysis which focuses on the evolution of discrete wavepackets while the addition of inflow noise is a form of continuous forcing. However, it seems plausible that at any instant the noise field could be projected onto the optimal perturbation modes to help describe its subsequent downstream evolution.

3.4.1. *Effect of upstream noise*

Blackburn *et al.* (2008*a*) examined the effect of background noise at inflow on the triggering of shedding from the separating shear layer for a backward-facing step. For the present flow, two-dimensional simulations were performed with the vertical inflow velocity component continuously perturbed, at each time step and at each grid point, using Gaussian noise for a range of standard deviations to determine the level required for sustained shedding. The actual root-mean-square (r.m.s.) noise level was then measured near the front of the plate. This was done for various Reynolds numbers and noise levels. Figure 19 shows the effect on the flow in the vicinity of the separation zone for different perturbation levels for $Re = 350$. At a r.m.s. noise level of 0.1 %, there is only a minor influence on the downstream flow although the effect of perturbing the flow is still quite noticeable. Increasing the r.m.s. noise level to 0.5 % results in shedding of vortices from the separation bubble. The effect is stronger as the noise level is increased to 1 %. Interestingly, as discussed previously, for experiments $Re = 350$ appears to be just past the upper limit of steady flow. These results are consistent with that observation. For instance, noise levels in water tunnels can be up to 1 % or more (Sasaki & Kiya 1991), and these results indicate that noise is amplified sufficiently at such an upstream noise level to sustain strong shedding of vortices from the shear layer.

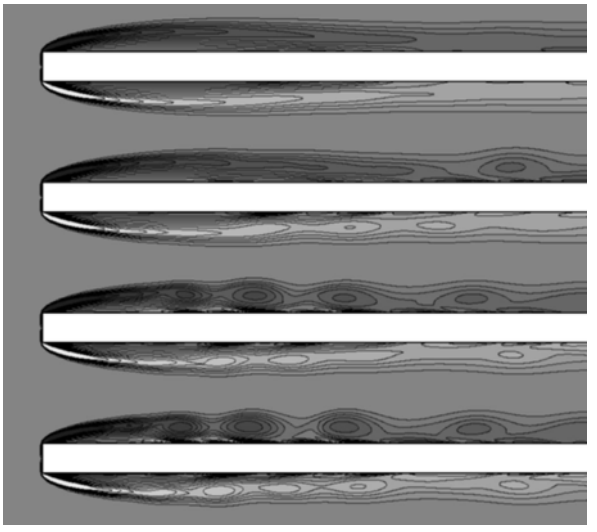

FIGURE 19. Typical vorticity patterns produced from different levels of upstream fluctuations for $Re = 350$. Top to bottom correspond to r.m.s. perturbation amplitudes of 0.1, 0.5, 1.0 and 2.0 %, respectively. The greyscale map and overlaid contours show spanwise vorticity. The downstream boundary is at $x = 20H$.

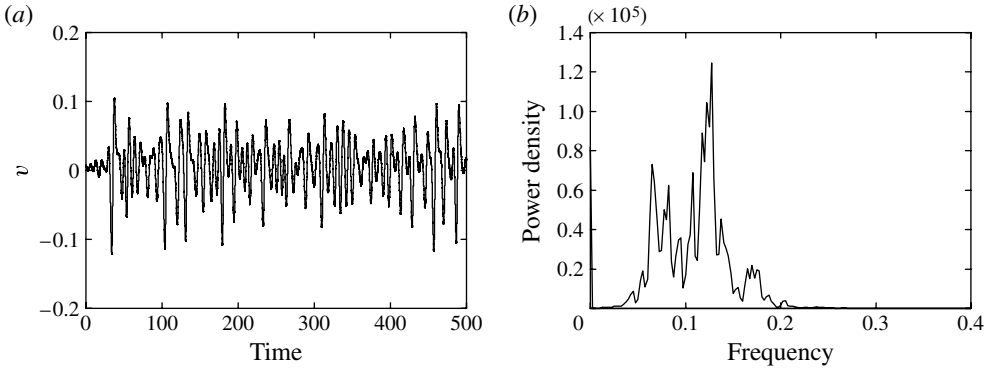

FIGURE 20. (*a*) Time series of the vertical velocity component well downstream of reattachment $(x, y) = (20.91, 1.32)$ showing velocity fluctuations as the shed vortices pass. (*b*) Power spectrum of the velocity component. This case corresponds to $Re = 350$ using a 1 % r.m.s. velocity perturbation.

Figure 20 shows a time sequence of the vertical velocity component well downstream of the separation bubble $(20.9H, 1.32H)$ together with the power spectrum of the signal. This is for $Re = 350$ at a 1 % noise level. The time signal shows considerable randomness but with a dominant frequency component shown in the power spectrum. The dominant peak corresponds to a frequency 0.125. This corresponds quite closely to the reciprocal of the time for the optimal perturbation mode wavepacket shown in figure 10 to advect forward through a single wavelength,

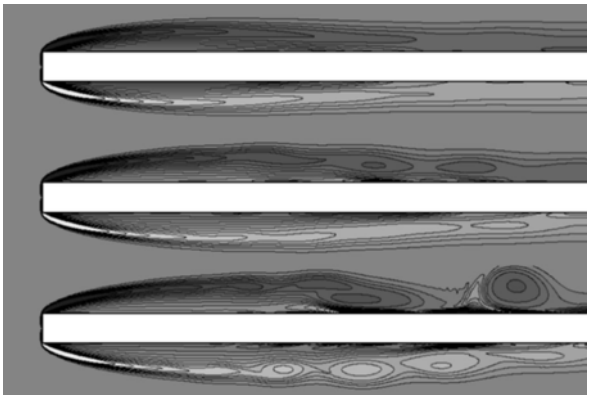

FIGURE 21. Typical vorticity patterns for a fixed perturbation amplitude of 0.1 % as the Reynolds number is varied. Top to bottom correspond to $Re = 350$, 400 and 450, respectively. The greyscale map and overlaid contours show spanwise vorticity. The downstream boundary is at $x = 20H$.

approximately eight time units, also giving $f = 1/8 = 0.125$. A similar match up was also found for the flow over a backward-facing step by Blackburn *et al.* (2008*a*).

Figure 21 shows the effect of changing the Reynolds number for fixed low-level inflow noise. For this case the r.m.s. noise was 0.1 %. Increasing the Reynolds number from $Re = 350$ to 400 and 450 shows that while there is minor downstream unsteadiness at $Re = 350$, for $Re = 450$ this very low level of upstream noise is sufficient to produce strong shedding. This is consistent with the optimal perturbation result of a 2.5 order-of-magnitude increase in energy amplification for each Reynolds number increment of 100.

4. Conclusions

A number of different experiments examining the flow over a blunt leading-edge long flat plate indicate that the separation bubble begins to shed vortices for Reynolds numbers in the range $260 < Re < 330$. The stability analysis presented here indicates that three-dimensional transition to steady flow only occurs at a higher Reynolds number closer to 400 and that the two-dimensional steady flow is global temporally stable up to a Reynolds number of approximately 500. Thus, it appears that the massive amplification of perturbations due to the non-normality of global instability modes may lead to effective early transition to unsteady three-dimensional flow. Of course, in the experiments quasi-periodic forcing may also contribute to the development of shedding of vortices, e.g. blade-passing perturbations from the pump or fan driving the flow, or the trailing-edge vortex feedback instability from vortex passing the trailing edge of the plate perturbing the upstream shear layer through a pressure pulse, or duct resonance (e.g. see Hourigan *et al.* 2001). However, even in these cases, the mechanism relies on the receptivity of the shear layer and the amplification of perturbations as they convect downstream. This is at least partially quantified through optimal perturbation mode analysis.

This paper quantifies the energy growth of optimal perturbation modes for this flow problem. At $Re = 350$, the energy amplification of the dominant optimal mode is greater than 10^4, and it increases by 2.5 decades for each 100 unit increase in Reynolds number. The optimal perturbation field is localized in the vicinity of the

leading-edge corners. This means that the projection of structured flow perturbations onto the optimal field can be significant. It is also shown that random noise at inflow can cause sustained vortex shedding from the recirculation bubble for a r.m.s. noise level of 0.5 % or more, with some unsteadiness detectable even with a 0.1 % noise level. Interestingly this ties in well with previous experiments where it has been observed that the recirculation bubble becomes unsteady in the range $260 < Re < 330$. Often r.m.s. turbulence levels in water tunnels can be up to 1 % or higher at the low Reynolds numbers relevant to this paper. For example, for the tunnel used by Sasaki & Kiya (1991) for their studies of the flow over a flat plate, the longitudinal turbulence level was 2 % at the lowest possible speed dropping to 0.5 % at the higher speeds. Mills *et al.* (2003) quote 0.1 % and Lang, Rist & Wagner (2004) give a level of 0.05 %. Thus, even with a well-designed facility and very careful experimentation, it may not be possible to maintain steady separating and reattaching flow at Reynolds numbers in the vicinity of 350, even though the flow is globally linearly stable until much higher Reynolds numbers.

The paper also examines the relationship of the evolved optimal perturbation modes to linear convective instability modes associated with the velocity profile at mid bubble. An interpretation is that the initial optimal perturbation distribution is determined so that it rapidly evolves towards the convective instability mode of the bubble as the perturbation is convected downstream. In this form it is amplified rapidly as it convects further downstream along the shear layer; indeed the transient growth rate is reasonably close to the value given from one-dimensional convective instability theory.

Of some interest, as noted in the introduction, Ehrenstein & Gallaire (2008) found that the flapping instability for the flow over a bump could be correlated with a set of temporal instability modes becoming unstable over a small Reynolds number range. The frequencies of the modes were separated by a constant increment, so that a combination of the modes will lead to beating. Both the dominant mode frequency and the constant frequency difference between the modes seemed to be well correlated with the observed shedding and beating frequencies from DNS. Cherubini *et al.* (2010) found similar behaviour for the flow separation induced by suction and blowing. For the current case, well-resolved direct simulations indicate that the two-dimensional steady flow remains stable up to Reynolds number of approximately 500. However, the investigation of the effect of noise at inflow indicates that at $Re = 350$ even a 0.1 % r.m.s. noise level is sufficient to trigger some unsteadiness of the separation bubble, due to substantial amplification of optimal modes. The optimal perturbation mode analysis shows that increasing the Reynolds number to the onset of global transition at 500, will increase the sensitivity to noise by a factor $\sqrt{(10^{2.5})^{150/100}} \simeq 75$, i.e. almost two orders of magnitude. Thus, to experimentally investigate this global transition would require a r.m.s. noise level of approximately 0.001 % or better, which is seemingly beyond expectations for water tunnels. From a different point of view, it suggests that experimentally at least, individual global temporal modes are not going to directly contribute to transition to unsteady flow, although they will contribute indirectly through contributing to optimal growth modes due to non-normality.

REFERENCES

ALAM, M. & SANDHAM, N. D. 2000 Direct numerical simulation of 'short' laminar separation bubbles with turbulent reattachment. *J. Fluid Mech.* **403**, 223–250.

BARKLEY, D., BLACKBURN, H. M. & SHERWIN, S. J. 2008 Direct optimal growth analysis for time steppers. *Intl J. Numer. Meth. Fluids* **57**, 1435–1458.

BARKLEY, D., GOMES, M. G. M. & HENDERSON, R. D. 2002 Three-dimensional instability in flow over a backward-facing step. *J. Fluid Mech.* **473**, 167–190.

BARKLEY, D. & HENDERSON, R. D. 1996 Three-dimensional Floquet stability analysis of the wake of a circular cylinder. *J. Fluid Mech.* **322**, 215–241.

BLACKBURN, H. M., BARKLEY, D. & SHERWIN, S. J. 2008*a* Convective instability and transient growth in flow over a backward-facing step. *J. Fluid Mech.* **603**, 271–304.

BLACKBURN, H. M., SHERWIN, S. J. & BARKLEY, D. 2008*b* Convective instability and transient growth in steady and pulsatile stenotic flow. *J. Fluid Mech.* **607**, 267–277.

BUTLER, K. M. & FARRELL, B. F. 1992 Three-dimensional optimal perturbations in viscous shear flow. *Phys. Fluids* A **4**, 637–650.

CHERUBINI, S., ROBINET, J.-CH. & PALMA, P. DE 2010 The effects of non-normality and nonlinearity of the Navier–Stokes operator on the dynamics of a large laminar separation bubble. *Phys. Fluids* **22**, 014102.

CHOMAZ, J.-M. 2005 Global instabilities in spatially developing flows: nonnormality and nonlinearity. *Ann. Rev. Fluid Mech.* **37**, 357.

CHORIN, A. J. 1968 Numerical solution of the Navier-Stokes equations. *Maths Comput.* **22**, 745–762.

DUŠEK, J., FRAUNÍE, P. & LE GAL, P. 1994 Local analysis of the onset of instability in shear flows. *Phys. Fluids* **6** (1), 172–186.

EHRENSTEIN, U. & GALLAIRE, F. 2008 Two-dimensional global low-frequency oscillations of a separating boundary layer flow. *J. Fluid Mech.* **614**, 315–327.

GALLAIRE, F., MARQUILLIE, M. & EHRENSTEIN, U. 2006 Three-dimensional transverse instabilities in detached boundary layers. *J. Fluid Mech.* **571**, 221–233.

GASTER, M. 1966 The structure and behaviour of laminar separation bubbles. *Tech. Rep.* AGARD Publication CP-4 on Flow Separation: Part II.

GRIFFITH, M. D., LEWEKE, T., THOMPSON, M. C. & HOURIGAN, K. 2008 Steady inlet flow in stenotic geometries: convective and absolute instabilities. *J. Fluid Mech.* **616**, 111–133.

GRIFFITH, M. D., THOMPSON, M. C., LEWEKE, T. & HOURIGAN, K. 2010 Convective instability in steady stenotic flow: optimal transient growth and experimental observation. *J. Fluid Mech.* **655**, 504–514.

HOURIGAN, K., THOMPSON, M. C. & TAN, B. T. 2001 Self-sustained oscillations in flows around long blunt plates. *J. Fluids Struct.* **15**, 387–398.

JONES, L. E., SANDBERG, R. D. & SANDHAM, N. D. 2008 Direct numerical simulations of forced and unforced separation bubbles on an airfoil at incidence. *J. Fluid Mech.* **602**, 175–207.

KAIKTSIS, L., KARNIADAKIS, G. E. & ORSZAG, S. A. 1991 Onset of three-dimensionality, equilibria, and early transition in flow over a backward-facing step. *J. Fluid Mech.* **231**, 501–528.

KAIKTSIS, L., KARNIADAKIS, G. E. & ORSZAG, S. A 1996 Unsteadiness and convective instabilities in two-dimensional flow over a backward-facing step. *J. Fluid Mech.* **321**, 157–187.

KARNIADAKIS, G. E., ISRAELI, M. & ORSZAG, S. A. 1991 High-order splitting methods of the incompressible Navier–Stokes equations. *J. Comput. Phys.* **97**, 414–443.

LANE, J. C. & LOEHRKE, R. I. 1980 Leading-edge separation from a blunt plate at low Reynolds number. *ASME J. Fluids Engng* **102** (11), 494–496.

LANG, M., RIST, U. & WAGNER, S. 2004 Investigations on controlled transition development in a laminar separation bubble by means of LDA and PIV. *Exp. Fluids* **36**, 43–52.

LEONTINI, J. S., THOMPSON, M. C. & HOURIGAN, K. 2007 Three-dimensional transition in the wake of a transversely oscillating cylinder. *J. Fluid Mech.* **577**, 79–104.

MAMUN, C. K. & TUCKERMAN, L. S. 1995 Asymmetry and Hopf-bifurcation in spherical Couette flow. *Phys. Fluids* **7** (1), 80–91.

MARQUET, O., LOMBARDI, M., CHOMAZ, J.-M., SIPP, D. & JACQUIN, L. 2009 Direct and adjoint global modes of a recirculation bubble: lift-up and convective non-normalities. *J. Fluid Mech.* **622**, 1–21.

MARQUET, O., SIPP, D., CHOMAZ, J.-M. & JACQUIN, L. 2008 Amplifier and resonator dynamics of a low-Reynolds-number recirculation bubble in a global framework. *J. Fluid Mech.* **605**, 429.

MARXEN, O. & RIST, U. 2010 Mean flow deformation in a laminar separation bubble: separation and stability characteristics. *J. Fluid Mech.* **660**, 37–54.

MILLS, R., SHERIDAN, J. & HOURIGAN, K. 2003 Particle image velocimetry and visualization of natural and forced flow around rectangular cylinders. *J. Fluid Mech.* **478**, 299–323.

NAKAMURA, Y., OHYA, Y. & TSURATA, H. 1991 Experiments on vortex shedding from flat plates with square leading and trailing edges. *J. Fluid Mech.* **222**, 437–447.

OHYA, Y., NAKAMURA, Y., OZONE, S., TSURUTA, H. & NAKAYAMA, R. 1992 A numerical study of vortex shedding from flat plates. *J. Fluid Mech.* **236**, 445–460.

OTA, T., ASANO, Y. & OKAWA, K. 1981 Reattachment length and transition of the separated flow over blunt flat plates. *Bull. JSME* **24** (192), 941–947.

OZONO, S., OHYA, Y., NAKAMURA, Y. & NAKAYAMA, R. 1992 Stepwise increase in the strouhal number for flows around flat plates. *Intl J. Numer. Meth. Fluids* **15**, 1025–1036.

PAULEY, L. L., MOIN, P. & REYNOLDS, W. C. 1990 The structure of two-dimensional separation. *J. Fluid Mech.* **220**, 397–411.

REDDY, S. C. & HENNINGSON, D. S. 1993 Energy growth in viscous channel flows. *J. Fluid Mech.* **252**, 209.

RYAN, K., THOMPSON, M. C. & HOURIGAN, K. 2005 Three-dimensional transition in the wake of elongated bluff bodies. *J. Fluid Mech.* **538**, 1–29.

SASAKI, K. & KIYA, M. 1991 Three-dimensional vortex structure in a leading-edge separation bubble at moderate Reynolds numbers. *J. Fluids Engng* **113**, 405–410.

SCHMID, P. 2007 Nonmodal stability theory. *Annu. Rev. Fluid Mech.* **39**, 129.

SCHMID, P. J. & HENNINGSON, D. S. 2002 On the stability of a falling liquid curtain. *J. Fluid Mech.* **463**, 163.

SHEARD, G. J., THOMPSON, M. C. & HOURIGAN, K. 2003 From spheres to circular cylinders: the stability and flow structures of bluff ring wakes. *J. Fluid Mech.* **492**, 147–180.

SHEARD, G. J., THOMPSON, M. C. & HOURIGAN, K. 2004 From spheres to circular cylinders: non-axisymmetric transition in the flow past rings. *J. Fluid Mech.* **506**, 45–78.

TAN, B. T., THOMPSON, M. C. & HOURIGAN, K. 1998 Simulated flow around long rectangular plates under cross flow perturbations. *Intl J. Fluid Dyn.* **2** (1).

TAN, B. T., THOMPSON, M. C. & HOURIGAN, K. 2004 Flow past rectangular cylinders: receptivity to transverse forcing. *J. Fluid Mech.* **515**, 33–62.

THOMPSON, M. C., HOURIGAN, K., CHEUNG, A. & LEWEKE, T. 2006 Hydrodynamics of a particle impact on a wall. *Appl. Math. Model.* **30**, 190–196.

THOMPSON, M. C., HOURIGAN, K. & SHERIDAN, J. 1996 Three-dimensional instabilities in the wake of a circular cylinder. *Exp. Therm. Fluid Sci.* **12**, 190–196.

THOMPSON, M. C., LEWEKE, T. & PROVANSAL, M. 2001*a* Kinematics and dynamics of sphere wake transition. *J. Fluids Struct.* **15**, 575–585.

THOMPSON, M. C., LEWEKE, T. & WILLIAMSON, C. H. K. 2001*b* The physical mechanism of transition in bluff body wakes. *J. Fluids Struct.* **15**, 607–616.

TREFETHEN, L. N., TREFETHEN, A. E., REDDY, S. C. & DRISCOLL, T. A. 1993 Hydrodynamic stability without eigenvalues. *Science* **261**, 578–584.